Horizontally Explicit and Vertically Implicit (HEVI) Time Discretization Scheme for a Discontinuous Galerkin Nonhydrostatic Model

LEI BAO

Department of Applied Mathematics, University of Colorado Boulder, Boulder, Colorado

ROBERT KLÖFKORN AND RAMACHANDRAN D. NAIR

National Center for Atmospheric Research,* Boulder, Colorado

ABSTRACT

A two-dimensional nonhydrostatic (NH) atmospheric model based on the compressible Euler system has been developed in the (x, z) Cartesian domain. The spatial discretization is based on a nodal discontinuous Galerkin (DG) method with exact integration. The orography is handled by the terrain-following height-based coordinate system. The time integration uses the horizontally explicit and vertically implicit (HEVI) time-splitting scheme, which is introduced to address the stringent restriction on the explicit time step size due to a high aspect ratio between the horizontal (x) and vertical (z) spatial discretization. The HEVI scheme is generally based on the Strang-type operator-split approach, where the horizontally propagating waves in the Euler system are solved explicitly while the vertically propagating waves are treated implicitly. As a consequence, the HEVI scheme relaxes the maximum allowed time step to be mainly determined by the horizontal grid spacing. The accuracy of the HEVI scheme is rigorously compared against that of the explicit strong stability-preserving (SSP) Runge–Kutta (RK) scheme using several NH benchmark test cases. The HEVI scheme shows a second-order temporal convergence, as expected. The results of the HEVI scheme are qualitatively comparable to those of the SSP-RK3 scheme. Moreover, the HEVI DG formulation can also be seamlessly extended to account for the second-order diffusion as in the case of the standard SSP-RK DG formulation. In the presence of orography, the HEVI scheme produces high quality results, which are visually identical to those produced by the SSP-RK3 scheme.

1. Introduction

With an increased amount of supercomputing resources available to present-day modelers, it is possible to develop global atmospheric models with horizontal grid resolution of the order of a few kilometers. At this fine resolution, the models require a set of nonhydrostatic (NH) governing equations in order to resolve clouds at a global scale (Tomita et al. 2008). However, this necessitates the development of spatial and temporal discretization schemes that are capable of facilitating excellent parallel efficiency

on peta-scale computers. Numerical schemes that can address these challenges should have computationally desirable *local* properties such as compact computational stencils, high on-processor operations, and minimal communication footprints. There is a renewed interest in developing new NH models based on finite-volume (FV; Ahmad and Linedman 2007; Norman et al. 2011; Skamarock et al. 2012; Ullrich and Jablonowski 2012; Li et al. 2013) and Galerkin methods (Giraldo and Restelli 2008; Giraldo et al. 2013; Brdar et al. 2013), which are designed to address these computational challenges to a great extent.

Among the emerging approaches for spatial discretization, the discontinuous Galerkin (DG) method stands out as a strong candidate, owing to its several computationally attractive features such as local and global conservation, high-order accuracy, high parallel efficiency, and geometric flexibility. The DG method may be viewed as a hybrid approach combining the desirable features of two standard numerical discretization approaches: FV

and the finite-element (spectral element) methods. The DG spatial discretization combined with Runge–Kutta (RK) time integration provides a class of robust algorithms known as the RKDG method for solving conservation laws (Cockburn 1997). The application of DG methods in atmospheric modeling is becoming increasingly popular in both hydrostatic (Nair et al. 2009) and NH modeling (Giraldo and Restelli 2008; Brdar et al. 2013). A recent review by Nair et al. (2011) presents various DG applications in atmospheric science with an extensive list of references. By virtue of the aforementioned advantages, we employ a DG method for the spatial discretization for a NH model based on the compressible Euler system in two dimensions (2D) on the x–z plane, under the terrain-following height-based coordinate system (Gal-Chen and Sommerville 1975); hereafter this is referred to as the DG-NH model.

The advantage of explicit time-stepping schemes is their simplicity and high parallel efficiency, namely, the minimal interprocessor communication, when evaluating the equations of motion (see, e.g., Dennis et al. 2012). Explicit strong stability-preserving (SSP)-RK time integration is typically used together with P^k-DG methods, which employ a set of polynomials of degree up to k, but results in a severe Courant–Friedrichs–Lewy (CFL) stability limit of $1/(2k + 1)$; note that this relationship is approximate for $k > 1$ [see Cockburn (1997)]. The penalizing drawback of this combination is that a numerical method that is high order in space requires a smaller time step size than the corresponding low-order variant with the same grid spacing. Besides, for the compressible NH system, the physically insignificant fast-moving sound waves dictate the explicit time step size, which imposes a stringent stability constraint on the whole system and impedes the computational efficiency. To make matters worse, the vertical grid spacing is several magnitudes smaller than the horizontal grid spacing ($\approx$1:1000) in a typical global atmospheric model. The vertical discretization with small grid spacing permits only a tiny explicit time step size, and atmospheric models based on this option have only a limited practical value. There are established models based on the anelastic or soundproof system of equations, which eliminates sound waves from the continuous system (Prusa et al. 2008). Nevertheless, the solution process of such models involves expensive elliptic solvers, and the ultimate efficiency of the model is tied up with that of the elliptic solvers and associated preconditioners. A fully implicit time-stepping approach might be devised to solve the compressible NH model (St-Cyr and Neckels 2009), but this again requires expensive implicit solvers. In general, the cost effectiveness (parallel efficiency) of models that rely upon global elliptic solvers, is not clear in a peta-scale computing environment.

The split-explicit and semi-implicit time stepping schemes are two possible alternatives that are widely used in many operational weather forecasting centers. Split-explicit methods fall into the subcycling category, where the shorter substeps are used for the faster-moving acoustic and gravity terms of the governing equations (Tomita et al. 2008). In semi-implicit models, acoustic and gravity waves are usually treated implicitly while the advection parts are solved explicitly (Durran 1999; Simarro et al. 2013). Consequently, the time step size is relaxed from the speed of sound and the gravity waves, which shows relatively better efficiency at the cost of a Helmholtz solver. Implicit–explicit (IMEX) schemes, a variant of semi-implicit schemes, treat the fast time-scale terms implicitly and the slow time-scale terms explicitly. Restelli and Giraldo (2009) studied IMEX time integrators used with the DG spatial discretization to improve the efficiency of the scheme by rewriting the problem in the form of a pseudo-Helmholtz operator.

The horizontal explicit and vertical implicit (HEVI) schemes are another type of splitting approach in which the terms responsible for the horizontal dynamics are solved explicitly while treating the vertical terms implicitly (Satoh 2002). Note that the HEVI scheme may be viewed as a framework where the IMEX time integration schemes can be incorporated. In a recent work, Weller et al. (2013) give a detailed comparison of popular options of HEVI time stepping schemes. For HEVI scheme the maximum time step size is only limited by the horizontal grid spacing and, this choice of time step is usually acceptable in the real application as shown in Skamarock and Klemp (2008) and Tomita et al. (2008). A linear analysis of various RK HEVI schemes can be found in Lock et al. (2014). Recently, there is a renewed interest on the applications of the HEVI schemes for high-order methods as used in NH modeling. Ullrich and Jablonowski (2012) examined three RK IMEX schemes for HEVI splitting of nonhydrostatic solutions using a FV spatial discretization, which includes the crude-splitting, Strang-carryover splitting and (Ascher–Ruuth–Spiteri) ARS(2, 3, 3) of Ascher et al. (1997). A novelty of Ullrich and Jablonowski (2012) is the recycling of the solution of the previous time step as the solution for the first implicit solution for the Strang-carryover scheme. The computational expense due to the implicit solver is optimized by using a Rosenbrock-type solver, which is essentially one Newton iteration. Giraldo et al. (2013) studied the accuracy and efficiency of IMEX methods, when discretized with continuous Galerkin methods, in semi-implicit and HEVI form for nonhydrostatic 3D flows (both on the globe and in the limited area).

In the present work, we investigate the performance of HEVI time-stepping method with the DG-NH model (hereafter referred to as HEVI-DG) using an operator-split approach. We also use the explicit SSP-RK method without time splitting for the DG-NH model to provide results for comparison. To extend the time step size with explicit RK methods, we employ moderate order P^k-DG where $k \leq 4$, with exact integration using Gauss–Legendre quadratures, which is different from the high-order formulation considered in Giraldo and Restelli (2008). The parallel version of the model is implemented with a horizontal domain decomposition that assumes that the vertical column (z direction) of data is not distributed across the processors. In this way, the vertical implicit solver does not need any interprocessor communication. Furthermore, we can take advantage of the existing knowledge of the IMEX-RK schemes to generate HEVI-DG schemes with the desired properties and temporal accuracy.

The organization of the paper is as follows. The governing equations and the computational forms are described in section 2. The DG spatial discretization is discussed in section 3, followed by the time integration schemes in section 4. The numerical results for several benchmark test cases are presented in section 5. Conclusions and some future work are described in section 6. The implementation of the diffusion process is detailed in the appendix.

2. The idealized nonhydrostatic model

The model is designed to simulate two-dimensional (2D) airflow over a (x, z) Cartesian domain. The compressible nonhydrostatic Euler system of equations can be written in the following vector form, without specifying the coordinate system:

$$\frac{\partial \rho}{\partial t} + \mathbf{\nabla} \cdot (\rho \mathbf{u}) = 0, \tag{1}$$

$$\frac{\partial \rho \mathbf{u}}{\partial t} + \mathbf{\nabla} \cdot (\rho \mathbf{u} \otimes \mathbf{u} + p\mathbf{I}) = -\rho g \mathbf{k}, \quad \text{and} \tag{2}$$

$$\frac{\partial \rho \theta}{\partial t} + \mathbf{\nabla} \cdot (\rho \theta \mathbf{u}) = 0, \tag{3}$$

where ρ is the air density, $\otimes$ is the tensor (outer) product, $\mathbf{k}$ is the basis vector in the z direction with unit length, $\mathbf{u} = (u, w)^{\mathrm{T}}$ is the velocity vector with the vertical component $w = \mathbf{u} \cdot \mathbf{k}$, p is the pressure, g is the acceleration due to gravity, $\mathbf{I}$ represents the 2×2 identity matrix, and $\mathbf{\nabla} \cdot$ is the divergence operator. The potential temperature θ is related to the real temperature T by $\theta = T(p_0/p)^{R_d/c_p}$. The above system is closed by the equation of state, $p = C_0(\rho \theta)^\gamma$, where $C_0 = R_d^\gamma p_0^{-R_d/c_v}$. The reference surface pressure $p_0 = 10^5\,\mathrm{Pa}$, and the

other thermodynamic constants are given by $\gamma = c_p/c_v$, $R_d = 287\,\mathrm{J\,kg^{-1}\,K^{-1}}$, $c_p = 1004\,\mathrm{J\,kg^{-1}\,K^{-1}}$, and $c_v = 717\,\mathrm{J\,kg^{-1}\,K^{-1}}$.

a. Terrain-following height-based coordinate

Accurate representation of terrain is very important for practical NH modeling where mountain lee waves are forced by the irregularities (topography) of the earth's surface. The height-based vertical coordinate is popular in many nonhydrostatic global models (Prusa et al. 2008; Tomita et al. 2008; Skamarock et al. 2012). The terrain-following height-based coordinate offers more flexibility and accuracy compared to pressure-based coordinates, and is free from time-dependent terrain metrics (Toy and Randall 2009). Although the DG method is capable of handling complex domain (Giraldo and Restelli 2008), we prefer to use the classical terrain-following height coordinates introduced by Gal-Chen and Sommerville (1975). Recently, more sophisticated terrain-following coordinate systems were developed (Schär et al. 2002; Klemp 2011) and will be considered for future development.

If $h = h(x)$ is the prescribed mountain profile and z_T is the top of the model domain, then the vertical z height coordinate can be transformed to the monotonic ζ coordinate using the following mapping:

$$\zeta = z_T \frac{z - h(x)}{z_T - h(x)}, \quad z(\zeta) = h(x) + \zeta \frac{z_T - h(x)}{z_T}; \quad h(x) \leq z \leq z_T. \tag{4}$$

This coordinate transformation invariably introduces tensor quantities and metric terms associated with mapping as described in Gal-Chen and Sommerville (1975), Clark (1977), and Satoh (2002). Following the standard notations (Satoh 2002), the Jacobian of the transformation is given by $\sqrt{G}$ and defined as

$$\sqrt{G} = \left(\frac{\partial z}{\partial \zeta}\right)_{x=\text{const}}, \quad G^{13} = \left(\frac{\partial \zeta}{\partial x}\right)_{z=\text{const}}, \tag{5}$$

where the Jacobian and the metric term G^{13} are independent of time. For an arbitrary scalar ψ, we have the following relation connecting (x, z) and (x, ζ) coordinate systems (Clark 1977),

$$\sqrt{G}\,\frac{\partial \psi}{\partial z} = \frac{\partial \psi}{\partial \zeta}, \tag{6}$$

$$\sqrt{G}\left[\frac{\partial \psi}{\partial x}\right]_{z=\text{const}} = \left[\frac{\partial}{\partial x}(\sqrt{G}\psi)\bigg|_{\zeta=\text{const}} + \frac{\partial}{\partial \zeta}(\sqrt{G}G^{13}\psi)\right]. \tag{7}$$

The vertical velocity in the transformed system (x, ζ) is $\tilde{w}$ and defined as

$$\tilde{w} = \frac{d\zeta}{dt} = \frac{1}{\sqrt{G}}(w + \sqrt{G}G^{13}u). \tag{8}$$

The divergence operation for a vector field $\mathbf{F} = (F^x, F^z)$ under the coordinate transformation takes the following form:

$$\nabla \cdot \mathbf{F} = \frac{1}{\sqrt{G}}\left[\frac{\partial}{\partial x}(\sqrt{G}F^x) + \frac{\partial}{\partial \zeta}(F^z + \sqrt{G}G^{13}F^x)\right]. \tag{9}$$

b. Removal of the hydrostatic balanced state

In the context of atmospheric modeling, it is common to write the thermodynamic variables as the sum of the mean state (reference state) $\overline{(\cdot)}$ and perturbation $(\cdot)'$ (Skamarock and Klemp 2008):

$$\rho(x, z, t) = \overline{\rho}(z) + \rho'(x, z, t), \tag{10}$$

$$\theta(x, z, t) = \overline{\theta}(z) + \theta'(x, z, t), \tag{11}$$

$$p(x, z, t) = \overline{p}(z) + p'(x, z, t), \quad \text{and} \tag{12}$$

$$(\rho\theta)(x, z, t) = \overline{\rho\theta}(z) + (\rho\theta)'(x, z, t), \tag{13}$$

where the mean state satisfies the hydrostatic balance:

$$\frac{d\overline{p}}{dz} = -\overline{\rho}g. \tag{14}$$

The mean-state part of the thermodynamic variables is in hydrostatic balance and makes no contribution to drive the dynamics. In contrast, the dynamic processes, or the accelerations, are triggered and influenced by the perturbation part (Clark 1977). Besides, the deviations due to the nonhydrostatic effect from the hydrostatic balance are relatively small, except for certain extreme cases such as tornadoes. Embodying the mean state in the whole system may introduce some errors in approximating the hydrostatic equilibrium numerically, which may generate some spurious vertical momentum. Therefore, the hydrostatically balanced mean state is removed from the Euler system.

c. Governing equations

Combining the relations (5)–(9) and substituting in the Euler system (1)–(3) results in the following general 2D Euler system in the transformed (x, ζ) coordinates:

$$\frac{\partial \mathbf{U}}{\partial t} + \frac{\partial \mathbf{F}^x(\mathbf{U})}{\partial x} + \frac{\partial \mathbf{F}^\zeta(\mathbf{U})}{\partial \zeta} = \mathbf{S}(\mathbf{U})$$

$$\Rightarrow \frac{\partial \mathbf{U}}{\partial t} + \nabla \cdot \mathbf{F}(\mathbf{U}) = \mathbf{S}(\mathbf{U}), \tag{15}$$

where $\mathbf{U}$ is the state vector and $\mathbf{U} = [\sqrt{G}\rho', \sqrt{G}\rho u, \sqrt{G}\rho w, \sqrt{G}(\rho\theta)']^T$, $\mathbf{S}$ is the source term, and $\mathbf{S} = [0, 0, -\sqrt{G}\rho'g, 0]^T$. The variables $\mathbf{F}^x$ and $\mathbf{F}^\zeta$ are the flux vectors along x and ζ directions, respectively, which have the following forms:

$$\mathbf{F}^x = \begin{bmatrix} \sqrt{G}\rho u \\ \sqrt{G}(\rho u^2 + p') \\ \sqrt{G}\rho uw \\ \sqrt{G}\rho u\theta \end{bmatrix}, \quad \mathbf{F}^\zeta = \begin{bmatrix} \rho\tilde{w} \\ \rho u\tilde{w} + \sqrt{G}G^{13}p' \\ \rho w\tilde{w} + p' \\ \rho\tilde{w}\theta \end{bmatrix},$$

$$\mathbf{S} = \begin{bmatrix} 0 \\ 0 \\ -\sqrt{G}\rho'g \\ 0 \end{bmatrix}, \tag{16}$$

and $\mathbf{F} = (\mathbf{F}^x, \mathbf{F}^\zeta)$. The compressible 2D Euler system in (15) is the basis for the DG-NH model. Note that in the absence of topography $[h(x) = 0, \zeta = z]$, we have $\sqrt{G} = 1$, $G^{13} = 0$ and $w = \tilde{w}$.

3. DG spatial discretization

The DG method is usually termed as a hybrid scheme, combining the best properties of the spectral element and FV methods. The application of DG methods in the atmospheric community is a vigorous research field [see Nair et al. (2011) for details], and we only provide a brief outline of the DG discretization process herein. Without loss of generality, we consider a scalar component of the Euler system in (15) without orography on a rectangular Cartesian domain $\mathcal{D}$ for DG spatial discretization:

$$\frac{\partial U}{\partial t} + \nabla \cdot \mathbf{F}(U) = S(U), \quad \text{in} \quad (0, t_T) \times \mathcal{D}; \quad \forall \quad (x, z) \in \mathcal{D}, \tag{17}$$

where $U = U(x, z, t)$, $\mathbf{F}$ is the flux function, and S is the source term; t_T is the prescribed time. Initially, $u_0(x, z) = u(x, z, t = 0)$ and suitable boundary conditions are imposed.

The DG spatial discretization procedure consists of partitioning the domain $\mathcal{D}$ into nonoverlapping $N_x \times N_z$ regular elements Ω_{ij}, such that

$$\Omega_{ij} = [x_{i-1/2}, x_{i+1/2}] \otimes [z_{j-1/2}, z_{j+1/2}],$$

$i = 1, \ldots, N_x, j = 1, \ldots, N_z$ and seeking an approximate solution U_h for U on each element, which satisfies that

$$U_h \in \mathcal{V}_h^k = [\varphi \in L^2(\mathcal{D}): \varphi|_{\Omega_{i,j}} \in \mathcal{P}_k(\Omega_{i,j}), \quad \forall \quad \Omega_{i,j} \in \mathcal{D}],$$

where $\mathcal{P}_k = \text{span}\{x^m z^n : 0 \le m, n \le k\}$. The aforementioned process is identical on each element, so we consider a generic element Ω_e herein.

a. Weak Galerkin formulation

Multiplying (17) by a test function $\varphi_h \in \mathcal{V}_h^k$ and integrating by parts over Ω_e leads to the following weak Galerkin formulation:

$$\frac{\partial}{\partial t}\int_{\Omega_e} U_h \varphi_h \, d\Omega - \int_{\Omega_e} \mathbf{F}(U_h) \cdot \nabla \varphi_h \, d\Omega + \int_{\Gamma_e} \hat{\mathbf{F}}(U_h) \cdot \mathbf{n}\varphi_h \, d\Gamma$$
$$= \int_{\Omega_e} S(U_h)\varphi_h \, d\Omega,$$
$$(18)$$

where $\mathbf{n}$ is the outward-facing unit normal vector of the edge Γ_e, and $\hat{\mathbf{F}}(U_h)$ is the numerical flux, which is crucial to resolve the discontinuity of the interelement solutions. In general, high-order DG schemes employing polynomials of degree up to k are often referred to as P^k-DG methods.

In (18), for simplicity and efficiency, the numerical flux is chosen as Lax–Friedrichs flux (Cockburn 1997):

$$\hat{\mathbf{F}}(U_h^+, U_h^-) = \frac{1}{2}\{[\mathbf{F}(U_h^-) + \mathbf{F}(U_h^+)] \cdot \mathbf{n} - \lambda_{\max}(U_h^+ - U_h^-)\},$$
$$(19)$$

where U_h^- and U_h^+ are the left and right limits, respectively, of the solution at the interface Γ_e. For the Euler system, $\lambda_{\max}$ is the upper bound on the absolute value of eigenvalues of the flux Jacobian $\mathbf{F}'(U)$, which is a function of the wind speed $\mathbf{u}$ and speed of sound waves c, evaluated at the interface:

$$\lambda_{\max} = \max\{|v^-| + c, |v^+| + c\}, \quad c = \sqrt{\gamma R_d T},$$
$$v^{\pm} = \mathbf{u}^{\pm} \cdot \mathbf{n}. \qquad (20)$$

b. Nodal basis functions

The integral equation (18) plays a central role in the DG discretization. The accuracy and efficiency of the scheme are greatly dependent on the particular choice for $\mathcal{V}_h^k$ and the quadrature rules chosen for the surface and line integrals.

In the current study, we are focusing only on *moderate* order P^k-DG discretization for the DG-NH model with $k \le 4$. Note that a major limitation of the DG scheme is the stringent CFL stability constraint associated with the explicit time stepping. Reducing the order of accuracy significantly improves the CFL stability restriction with explicit time stepping and, therefore, allows for implementation of limiting (positivity preserving) algorithms,

based on those designed for FV methods (Zhang and Nair 2012).

To solve the weak form (18), we introduce an affine mapping from each Ω_e to a reference element $\Omega_Q = [-1, 1]^2$, which simplifies the integrals in (18):

$$\xi = \frac{2(x - x_i)}{\Delta x_i}, \quad \Delta x_i = (x_{i+1/2} - x_{i-1/2}), \quad \text{and} \quad (21)$$

$$\eta = \frac{2(z - z_j)}{\Delta z_j}, \quad \Delta z_j = (z_{j+1/2} - z_{j-1/2}), \qquad (22)$$

where $(\xi, \eta) \in \Omega_Q$ are local independent variables, and $x_i = (x_{i+1/2} + x_{i-1/2})/2$ and $z_j = (z_{j+1/2} + z_{j-1/2})/2$.

For the computational efficiency, the nodal DG discretization is employed in the present work. The Lagrange polynomials $\{h_l(\xi)\}_{l=0}^k$ are adopted as the basis functions, the roots of which are a set of the chosen Gauss quadrature points (Karniadakis and Sherwin 2005), and they satisfy the discrete orthogonal properties:

$$h_l(\xi_m) = \delta_{lm}, \quad \text{and}$$

$$\int_{-1}^1 h_l(\xi)h_m(\xi) \, d\xi \simeq w_l \delta_{lm},$$

where w_l are the weights associated with the quadrature rule and δ_{lm} is the Kronecker function ($\delta_{lm} = 0$ if $l \ne m$, $\delta_{lm} = 1$ if $l = m$).

There are a range of choices for the quadrature rules, among which Gauss–Legendre (GL) and Gauss–Lobatto–Legendre (GLL) quadrature rules are the most popular (Nair et al. 2011). For P^k-DG methods, the GL quadrature rule provides the exact integration of (18), which is suitable for a moderate order (p^k, $k = 2, 3$, 4) of approximation. The GL grid is chosen for the present development. A schematic plot of the grids with 3×3 and 4×4 GL quadrature points is shown in Fig. 1. For the GL grid with the quadrature points $\{\xi_m\}_{m=0}^k$, the Lagrange polynomial $\{h_l(\xi)\}_{l=0}^k$ and the corresponding weight are given as

$$h_l(\xi)|_{GL} = \frac{P_{k+1}(\xi)}{P'_{k+1}(\xi_l)(\xi - \xi_l)},$$
$$w_l|_{GL} = \frac{2}{(1 - \xi_l^2)[P'_{k+1}(\xi_l)]^2}, \qquad (23)$$

where $P_k(\xi)$ is the kth degree Legendre polynomial and $P'_k(\xi)$ is its derivative. Figure 1 shows these polynomials for $k = 2, 3$.

For 2D problems, as in the case of the DG-NH model, we use a tensor product of the basis functions, which is the basis set $\{h_l(\xi)h_m(\eta)\}$, where $l, m = 0, 1, \ldots, k$. In

(a) P²-DG and its basis functions
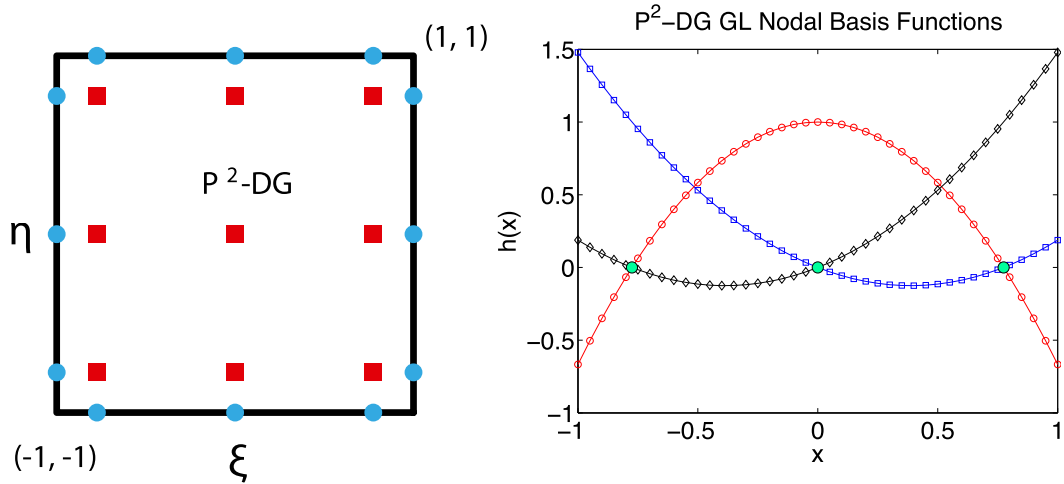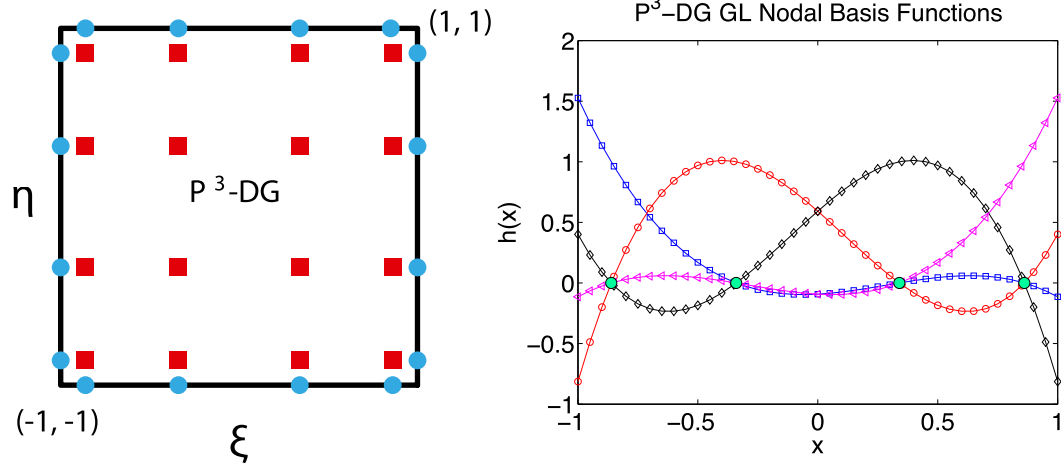

(b) P³-DG and its basis functions

FIG. 1. The reference element and the corresponding Lagrange polynomials with roots at (a) 3×3 and (b) 4×4 Gauss–Legendre (GL) points. Values at the flux points (filled round) are computed from the interior points by 1D interpolation along the ξ or η coordinate direction.

this way, the approximate solution $[U_h(\xi, \eta, t)]$ and the test function $\varphi_h(\xi, \eta)$ are expressed as

$$U_h(\xi, \eta, t) = \sum_{l=0}^{k} \sum_{m=0}^{k} U_{lm}(t) h_l(\xi) h_m(\eta), \quad \text{and} \quad (24)$$

$$\varphi_h(\xi, \eta) = h_l(\xi) h_m(\eta),$$

where $-1 \leq \xi, \eta \leq 1$ and $U_{lm}(t)$ denotes the nodal (grid point) values of the approximate solution U_h at time t.

c. Diffusion process

The design of the diffusion scheme is primarily based on the model's spatial discretization. There are various approaches to invoke diffusivity in atmospheric models,

and the most popular choice is the second-order explicit diffusion (∇^2). The local discontinuous Galerkin (LDG) method (Cockburn and Shu 1998), which takes inter-element contributions into account when treating the diffusion term (Laplacians), shows better consistency in addressing the discontinuous nature of the discretization (Nair 2009; Bao et al. 2014). We employ certain special cases of second-order LDG diffusion in our DG-NH model. The details of the implementation of the diffusion process can be found in the appendix.

d. Final form after DG spatial discretization

The final form of the spatial discretization, starting from the conservation law (17) via the weak form (18), leads to an ODE for each $U_{lm}(t)$:

$$\frac{d}{dt}U_{lm}(t) = \frac{4}{\Delta x_i \Delta z_j w_i w_j}[I_{\text{Grad}} + I_{\text{Flux}} + I_{\text{Source}}], \qquad (25)$$

where the coefficients $4/(\Delta x_i \Delta z_j w_i w_j)$ constitute the inverted mass matrix for an element Ω_{ij}. The term I_{Flux} is the line integral and, I_{Grad} and I_{Source} are the surface integrals corresponding to the discretization of the weak form in (18). Explicit definitions of these terms are given in Nair et al. (2011). Therefore, the ODE in time corresponding to the scalar conservation law (17) is

$$\frac{d}{dt}U_h(t) = \mathcal{L}(U_h), \qquad (26)$$

and for system (15) is

$$\frac{d}{dt}\mathbf{U}_h(t) = \mathbf{L}(\mathbf{U}_h), \qquad (27)$$

where $\mathcal{L}$ (or $\mathbf{L}$) indicates the spatial DG discretization.

4. Time integration procedure

In the construction of high-order RKDG methods (hereafter, we use DG for RK-DG), the spatial terms are discretized first, and the resulting ODE system for the prognostic variables is solved by a proper time integration scheme. The DG spatial discretization of the Euler system is fairly standard, which is elaborated on in section 3; however, the design of an efficient time integrator is of predominant importance, especially when we reach the nonhydrostatic scale.

We discuss the time integrator for an ODE system in the following general form:

$$\mathbf{U}'(t) = f[\mathbf{U}(t), t] \quad \text{in} \quad (0, t_T], \qquad (28)$$

where $\mathbf{U}(t)$ are the coefficients to the DG solution $\mathbf{U}_h(t)$ in (24). For the Euler's system in (27), the right-hand side function f is given by

$$f[\mathbf{U}(t), t] = \mathbf{L}[\mathbf{U}_h(t)]. \qquad (29)$$

In this paper, we investigate a HEVI-type splitting approach and compare it with commonly used explicit time stepping methods. All the time integrators considered in our development may be characterized as RK-type methods.

a. RK methods

Given the solution U^n at time t^n, we use an s-stage RK method to obtain the solution at the next time level t^{n+1}. For a given U^n and some integer $s > 0$, the coefficients $A \in \mathbb{R}^{s \times s}$, $b \in \mathbb{R}^s$, and $c \in \mathbb{R}^s$ define the s-stage RK method:

$$K_i = f\left(t^n + c_i \Delta t, U^n + \Delta t \sum_{j=1}^{2} A_{ij} K_j\right), \quad i = 1, \ldots, s,$$

$$U^{n+1} = U^n + \Delta t \sum_{i=1}^{s} b_i K_i. \qquad (30)$$

The coefficients $\mathbf{A} = [A_{ij}]$, $\mathbf{b} = [b_i]$, and $\mathbf{c} = [c_j]$ form the so-called Butcher tableau (Butcher 1987):

$$\begin{array}{c|c} \mathbf{c} & \mathbf{A} \\ \hline & \mathbf{b}^{\mathrm{T}} \end{array}.$$

For an explicit RK method, $A_{ij} = 0$ for all $j \geq i$, which corresponds to all entries of $\mathbf{A}$ on and above the diagonal being zero. Some popular examples of explicit SSP-RK methods (Gottlieb et al. 2001), which are widely used with the DG discretization (Nair et al. 2011), are as follows:

- Heun's method (SSP-RK2)

  (two-stage second order)

$$\begin{array}{c|cc} 0 & 0 & \\ 1 & 1 & 0 \\ \hline & \frac{1}{2} & \frac{1}{2} \end{array}.$$

- Explicit Runge–Kutta (SSP-RK3)

  (three-stage third order)

$$\begin{array}{c|ccc} 0 & 0 & & \\ 1 & 1 & 0 & \\ \frac{1}{2} & \frac{1}{4} & \frac{1}{4} & 0 \\ \hline & \frac{1}{6} & \frac{1}{6} & \frac{2}{3} \end{array}.$$

For implicit RK methods, we consider diagonally implicit RK (DIRK; Alexander 1977) methods. DIRK methods are characterized by the fact that the coefficients $A_{ij} = 0$ for $j > i$, in which case, all entries of $\mathbf{A}$ above the diagonal are zero. DIRK methods have the advantage that the resulting nonlinear systems can be solved one by one. A popular DIRK method is given below (Alexander 1977):

- Crank–Nicholson (DIRK2)

  (one-stage second order)

$$\begin{array}{c|c} \frac{1}{2} & \frac{1}{2} \\ \hline & 1 \end{array}.$$

For the solution of the nonlinear system for each RK stage, which arises due to the nonzero diagonal entries of **A** in (30), we apply a Jacobian-free Newton–Krylov (JFNK) method (Knoll and Keyes 2004). A generalized minimal residual (GMRES) (Saad and Schultz 1986) solver is applied for the linear system in each Newton step and the application of the right-hand-side operator f in each GMRES iteration is accomplished in a matrix-free fashion.

Explicit time integrators are relatively easy to implement and usually possess excellent parallel scalability. However, the general drawback with the application of explicit SSP-RK methods in DG methods is the severe time step restrictions (i.e., a CFL number much smaller than 1 has to be used). For the P^k-DG algorithm, a heuristic estimation of the CFL number is given by Cockburn (1997):

$$\frac{C\Delta t}{h} < \frac{1}{2k+1}, \tag{31}$$

where $h = \min\{\Delta x, \Delta z\}$, where Δz denotes the grid spacing in vertical direction and Δx the grid spacing in horizontal direction, and $C = \max\{|u| + c, |w| + c\}$, $c = \sqrt{\gamma R_d T}$ is the speed of sound. The resulting time step size for an explicit time integration scheme is usually very tiny. In contrast, the implicit ODE solver has a large stability region, which admits a large time step size, but is expensive to solve in general. The construction of the implicit solver for multidimensional problems is usually complicated and requires complex nonlinear solvers. The overall efficiency may not be competitive with the explicit solver and the computational scalability may even be degraded if the nonlinear solver is not designed properly. The hope of an efficient time integrator, which enables a large time step size and excellent computational efficiency, has triggered a vast research effort into implicit and semi-implicit time integration methods.

b. Horizontally explicit and vertically implicit (HEVI) scheme via Strang splitting

A popular approach in atmospheric applications is the HEVI approach. This is justified by the relatively large difference of scales in the horizontal and vertical directions (i.e., $\Delta z \ll \Delta x$). Although a large Δx still results in an acceptable CFL restriction for the present study, the small Δz introduces noticeable difficulties due to the severe CFL restriction in the vertical direction. As a result, a splitting approach with an implicit treatment in the vertical direction stands out as a suitable alternative. The horizontal direction is still treated explicitly, allowing the usage of the excellent scaling behavior of explicit methods. For the practical atmospheric applications, the horizontal CFL condition can be further

relaxed by subcycling or multirate integrations (Tomita et al. 2008), which is beyond the scope of the present work.

In our development, the domain decomposition for parallel computations is carried out in the horizontal direction only, which is broadly embraced in the atmospheric community (Michalakes et al. 2007). Therefore, all data is locally accessible in the vertical direction and an implicit treatment in the vertical direction does not require any communication. As a consequence, we expect the excellent scaling performance on today's many core systems to be maintained.

We split the DG spatial operator **L** in (27) into a horizontal (x) and a vertical (z) part such that

$$\mathbf{L}(\mathbf{U}_h) = \mathbf{L}^x(\mathbf{U}_h) + \mathbf{L}^z(\mathbf{U}_h), \tag{32}$$

where $\mathbf{L}^x$ and $\mathbf{L}^z$ are the DG 1D discretization to (33) and (34), respectively:

$$\frac{\partial \mathbf{U}_h}{\partial t} = -\frac{\partial \mathbf{F}^x(\mathbf{U}_h)}{\partial x} + \mathbf{S}^x, \quad \text{and} \tag{33}$$

$$\frac{\partial \mathbf{U}_h}{\partial t} = -\frac{\partial \mathbf{F}^z(\mathbf{U}_h)}{\partial z} + \mathbf{S}^z. \tag{34}$$

Note that, for the dimensional splitting used here, the source term is decomposed as $\mathbf{S}^x = 0$ and $\mathbf{S}^z = \mathbf{S}$. The definitions of $\mathbf{F}^x$, $\mathbf{F}^z$, and $\mathbf{S}$ are given in (16). Instead of solving the full system (28), we solve the system in the horizontal direction (33) and the system in the vertical direction (34) separately in a sequence, via the Strang-type splitting (Strang 1968). Strang-type splitting has been successfully applied in FV methods (Norman et al. 2011; Ullrich and Jablonowski 2012) and it also shows promising performances when applied to semi-Lagrangian DG methods for different geometries by Guo et al. (2014). Given a time interval of size Δt and the solution $\mathbf{U}_h^n$ at t_n, the corresponding Strang-splitting scheme has the following steps:

$$\mathbf{U}_0 = \mathbf{U}_h^n, \tag{35}$$

$$\frac{d}{dt}\mathbf{U}_1 = \mathbf{L}^x(\mathbf{U}_1) \quad \text{in} \quad (t^n, t^n + \Delta t/2],$$
$$\mathbf{U}_1(t^n) = \mathbf{U}_0, \tag{36}$$

$$\frac{d}{dt}\mathbf{U}_2 = \mathbf{L}^z(\mathbf{U}_2) \quad \text{in} \quad (t^n, t^{n+1}],$$
$$\mathbf{U}_2(t^n) = \mathbf{U}_1(t^n + \Delta t/2), \tag{37}$$

$$\frac{d}{dt}\mathbf{U}_3 = \mathbf{L}^x(\mathbf{U}_3) \quad \text{in} \quad (t^n + \Delta t/2, t^{n+1}],$$
$$\mathbf{U}_3(t^n + \Delta t/2) = \mathbf{U}_2(t^{n+1}), \quad \text{and} \tag{38}$$

$$\mathbf{U}_h^{n+1} = \mathbf{U}_3(t^{n+1}). \tag{39}$$

This approach requires the solution of the three equations, (36)–(38), which means that the horizontal part is solved for twice and the vertical part once (H-V-H). It would also be possible to solve the system in V-H-V form, but ideally the more expensive system should only be solved once. In our choice, we only solve the vertical system once. We also tested the Strang-carryover scheme (Ullrich and Jablonowski 2012), which is essentially V-H-V, with the first stage in the vertical is recycled from the previous time step; however, the solution is found to be degraded, even for a smooth test case.

Since we usually prefer higher order in the DG spatial discretization, the time integrator will be the dominant factor in the numerical error. Strang-type splitting permits second-order temporal accuracy (Toro 1999), therefore, we choose SSP-RK3 as the explicit time integrator for the horizontal direction (33) and we solve the vertical direction (34) either with the explicit RK method SSP-RK2, which leads to an horizontal explicit and vertical explicit (HEVE) method, for comparison studies, or with an implicit time stepping method DIRK2, which is our HEVI scheme. Therefore, the time integration schemes studied in the present paper are given as follows:

HEVI (or HEVE) time integrator

1) Solve (36) via SSP-RK3,
2) Solve (37) via DIRK2 (or SSP-RK2), and
3) Solve (38) via SSP-RK3.

The introduction of the HEVE time integration scheme is solely for the purpose of validating the idea of dimensional splitting for DG methods and, in practice, we would adopt the HEVI scheme for practical applications. When using an implicit method for the vertical direction (34), it is observed that the CFL condition for the whole system may be relaxed to the CFL condition for the horizontal part only. In other words, Δt for the Strang-splitting can be chosen as the largest possible Δt of (33). In this way, the overall performance can be greatly accelerated. Nevertheless, the necessity of solving an implicit system introduces an additional overhead. In terms of the performance of the DIRK methods, usually the number of Newton iterations is very small (i.e., 1 or 2 and usually not higher than 5). Therefore, the performance of the implicit solver is closely related to the number of iterations of the linear solver. This can be reduced by proper preconditioning. However, in the current implementation, no preconditioning is applied. The construction of a proper preconditioning method is ongoing work. In addition, because of our domain decomposition, we obtain an implicit system for each vertical column, which is decoupled for the other column systems. Therefore, no communication is needed for the implicit solvers. Even a direct solver could be applied since the system for one column is not that large. This will overcome the need for preconditioning the iterative solvers used otherwise.

The existing IMEX schemes (Ascher et al. 1997; Giraldo et al. 2013) can be easily incorporated into the HEVI-DG framework, which may yield some beneficial properties. To apply an IMEX time integrator, we first rewrite our problem such that we distinguish between a part that should be treated implicitly, here $\mathbf{L}^{im}$, and a part that should be treated explicitly, here $\mathbf{L}^{ex}$, such that

$$\frac{d}{dt}\mathbf{U}_h = \mathbf{L}^{im}(\mathbf{U}_h) + \mathbf{L}^{ex}(\mathbf{U}_h) \quad \text{in} \quad (t_n, t_{n+1}]. \quad (40)$$

For the IMEX RK method, we define $f^{im}[\mathbf{U}(t), t] = \mathbf{L}^{im}[\mathbf{U}(t)]$ and $f^{ex}[\mathbf{U}(t), t] = \mathbf{L}^{ex}[\mathbf{U}(t)]$. The performance of IMEX schemes combined with DG spatial discretization may be revisited in a future study.

5. Numerical experiments

To demonstrate and evaluate the HEVI time integration scheme in the DG-NH model, we choose several standard benchmark tests from the literature. Before detailing with each test case, we briefly discuss some common features such as the grid resolution, boundary conditions, and the initialization process used in the DG-NH model.

a. Numerical experiments setup

The spatial resolution should take account of the grid spacing within each element for the nodal DG (RK-DG) method. For the GL case, the edge points of each element are not included as solution points (see Fig. 1); therefore, we use an approximate procedure to define the minimum grid spacing for the P^k-DG method, which has $k + 1$ degrees of freedom (dof) in each direction. The *average* grid spacing is defined in terms of dof as

$$\Delta x = \Delta x_i/(k + 1), \quad \Delta z = \Delta z_j/(k + 1), \quad (41)$$

where Δx_i and Δz_j are the element width in the x direction and z direction, respectively [(21) and (22)]. We employ uniform elements over the whole domain, and use this convention in (41) as the grid resolution in our DG-NH model. Note that our definition of grid spacing is similar to Brdar et al. (2013) but different from that of Giraldo and Restelli (2008), where they use the GLL grid. The DG-NH model, designed for a rectangular domain, requires suitable boundary conditions for various test cases. These include no-flux, periodic, and nonreflecting type boundary specifications.

1) NO-FLUX BOUNDARY CONDITIONS

Essentially, the no-flux (or reflecting) boundary conditions eliminate the normal velocity component to the

boundary and only keep the tangential component. For an arbitrary velocity vector $\mathbf{v}$, the no-flux boundary condition results in $\mathbf{v} \cdot \mathbf{n} = 0$, where $\mathbf{n}$ is the outdrawn normal vector from the boundary. We denote $(v^{\parallel}, v^{\perp})$ as the parallel (tangential) and perpendicular (normal) components, respectively, of $\mathbf{v}$ along the boundary wall; let the left and right values at the element edge of $\mathbf{v}$ along the boundary be v_L and v_R, respectively. Then the no-flux boundary conditions can be written in the following form:

$$v_R^{\perp} = -v_L^{\perp}, \quad v_R^{\parallel} = v_L^{\parallel}. \tag{42}$$

The same idea is used for the flux vectors along the boundary.

2) NONREFLECTING BOUNDARY CONDITIONS

The nonreflecting (or transparent) boundary conditions are used to prevent the reflected waves from reentering the domain, which may interfere or pollute the flow structure. For the mountain test cases, nonreflecting boundary conditions are commonly imposed at the top (z_T) and the lateral boundaries, by introducing the sponge (absorbing) layers of finite width as discussed in Durran and Klemp (1983). We use a simple damping function as given below, and the damping terms will act as an additional forcing to the governing equations in (15). The prognostic vector $\mathbf{U}$ is then damped by relaxing to its initial state $\mathbf{U}_0$.

In the presence of orography, the governing equations become

$$\frac{\partial \mathbf{U}}{\partial t} = \cdots - \tau(x, z)(\mathbf{U} - \mathbf{U}_0), \tag{43}$$

where $\tau(x, z)$ is the sponge function, and at the upper boundary it is defined as (Melvin et al. 2010)

$$\tau(x, z) = \begin{cases} 0, & \text{if} \quad z_T - z \geq z_D, \\ \tau_{\text{top}} \left[\sin\left(\frac{\pi}{2} \frac{|z_T - z| - z_D}{z_D} \right) \right]^4 & \text{otherwise}, \end{cases} \tag{44}$$

where τ_{top} is the specified sponge coefficient and z_D is the thickness of the sponge zone from the domain boundary z_T in the z direction. The sponge function is accountable for the strength of damping over the zone. Similarly, for the lateral boundaries sponge functions can be defined with sponge coefficient τ_{lat}. In the overlap region (top corners), we use the maximum of the co-efficients in the x and z directions. The damping term in (44) has no effect on the interior part of the domain. Note that the magnitude of sponge thickness z_D, τ_{top},

and τ_{lat} is model dependent, a choice of which is in fact a trade-off between computational expense and the quality of the solution.

3) INITIAL CONDITIONS

For the DG-NH model, we use several standard conversion formulas for model initialization and maintain the hydrostatic balance. To initialize the hydrostatic balance, we obtain a vertical profile for the Exner pressure π, which is a function of pressure, given as

$$\pi = \left(\frac{p}{p_0} \right)^{R_d / c_p}, \tag{45}$$

which follows the hydrostatic balance:

$$\frac{d\pi}{dz} = -\frac{g}{c_p \theta}. \tag{46}$$

For some of the tests, a constant Brunt–Väisälä frequency N_f is specified and, therefore, $\overline{\theta}(z)$ can be computed from the following formula:

$$N_f^2 = g \frac{d}{dz}(\ln \overline{\theta}) \quad \Rightarrow \quad \overline{\theta}(z) = \theta_0 \exp\left(\frac{N_f^2}{g} z \right), \tag{47}$$

where θ_0 is a given constant. Once $\overline{\theta}(z)$ is known, the hydrostatically balanced Exner pressure in (45) can be derived as below:

$$\begin{aligned} \overline{\pi}(z) &= 1 + \frac{g^2}{c_p \theta_0 N_f^2} \left[\exp\left(-z \frac{N_f^2}{g} \right) - 1 \right] \\ &= 1 - \frac{g^2}{c_p N_f^2} \left[\frac{\overline{\theta}(z) - \theta_0}{\overline{\theta}(z)\theta_0} \right]. \end{aligned} \tag{48}$$

Another useful formula for computing $\overline{\rho}$ from $\overline{\pi}$ by using the conversion $\overline{T} = \overline{\theta}(z)/\overline{\pi}(z)$ is

$$\overline{\rho} = \frac{p_0}{R_d \overline{T}} \overline{\pi}^{(c_p / R_d)}. \tag{49}$$

For better visualization, the numerical results obtained from the DG-NH model simulations on the GL grid are bilinearly interpolated onto a high-resolution uniform grid.

b. Idealized NH test cases

We consider several NH benchmark test cases with varying complexities for validating the DG-NH model with HEVI time stepping. Except for the first test, all other test cases have no analytical solution and will, therefore, be evaluated qualitatively.
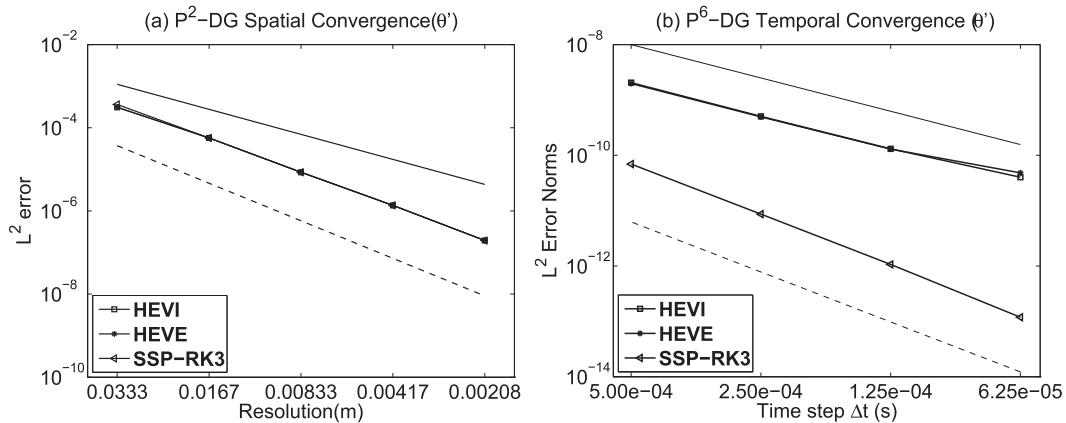
FIG. 2. The convergence plots for traveling sine-wave test with grid spacing $\Delta x = \Delta z$. (a) The h convergence of P^2-DG, with the SSP-RK3, HEVI, and HEVE integrators. (b) The t convergence of P^6-DG, with SSP-RK3, HEVI, and HEVE integrators. For both plots, the top solid line corresponds to the slope of second-order convergence and the bottom dashed line denotes the slope of third-order convergence (see the text for the grid-spacing details).

1) TRAVELING SINE-WAVE TEST

To study the convergence of the HEVI scheme, we consider a test case where an analytical solution is available for the Euler equations. This test case is described in Liska and Wendroff (2003), but we use a slight modification for the velocity and pressure suitable for our application. This test case simulates the traveling of sine waves at a nonhydrostatic scale on a square domain $[0, 1] \times [0, 1]\,\mathrm{m}^2$, where the waves march along the diagonal direction. The constant wind fields $\mathbf{u} = (u_0, w_0)$ are defined as

$$u_0(x, z, t) = \sin\frac{\pi}{5}, \quad w_0(x, z, t) = \cos\frac{\pi}{5}. \qquad (50)$$

The pressure p is set to be a constant 0.3 Pa, and the density is given as follows:

$$\rho(x, z, t) = \begin{cases} 0.5 & \text{if } R > 1.0, \\ 0.25\{\cos[\pi R(x, z, t)] + 1.0\}^2 + 0.5 & \text{else}, \end{cases} \qquad (51)$$

where $R(x, z, t) = 16[(x - 0.5 - ut)^2 + (z - 0.5 - wt)^2]$. The initial condition can be obtained by setting $t = 0\,\mathrm{s}$. Periodic boundary conditions are imposed for all four boundaries, and the simulation time is $t_T = 0.1\,\mathrm{s}$. To fit the governing equations in (15), the hydrostatically balanced variables $(\overline{\rho}, \overline{p}, \overline{\theta})$ are all set to zero. We neglect the influence of gravity and set the source term S in (16) to zero.

This test case mainly serves as a tool for the convergence study for the HEVI (or HEVE) scheme. For the tests a uniform grid with $\Delta x = \Delta z$ is chosen, regardless of the resolution. The L^2 error norms of HEVE, HEVE, and SSP-RK3 schemes are presented in Fig. 2, to show spatial errors (left panel) and temporal errors (right panel). To obtain the spatial convergence of the P^2-DG with respect to different time integration schemes, a reference solution is computed from the analytical solution at 0.1 s. The grid spacing Δz is halved (i.e., by doubling N_x and N_z) from $3.33 \times 10^{-2}\,\mathrm{m}$ ($N_x = 10$, $N_z = 10$) to $4.17 \times 10^{-3}\,\mathrm{m}$ ($N_x = 80$, $N_z = 80$); and Δt is set to $5.0 \times 10^{-4}\,\mathrm{s}$ for $\Delta z = 3.33 \times 10^{-2}\,\mathrm{m}$ initially, and decreased linearly with Δz. It

is observed that HEVI, HEVE, and SSP-RK3 show $\mathcal{O}(\Delta z^3)$ convergence, which is in line with the theoretical analysis for the DG spatial discretization.

To obtain the temporal convergence, we choose high-order P^6-DG to make the temporal error dominant over spatial errors. The grid resolution is set to $7.143 \times 10^{-3}\,\mathrm{m}$ ($N_x = 20$, $N_z = 20$), and Δt is decreased to obtain the trend of temporal errors. The reference solution is computed from $\Delta t = 3.125 \times 10^{-5}\,\mathrm{s}$ and Δt is halved from 5×10^{-4} to $6.25 \times 10^{-5}\,\mathrm{s}$. The L^2 error norms of all three time integrators are plotted in the right panel of Fig. 2. We observe that SSP-RK3 shows third-order temporal convergence. Both HEVI and HEVE only achieve second-order temporal convergence because the numerical errors of HEVI and HEVE are controlled by the second-order splitting errors.

2) INERTIA–GRAVITY WAVE TEST

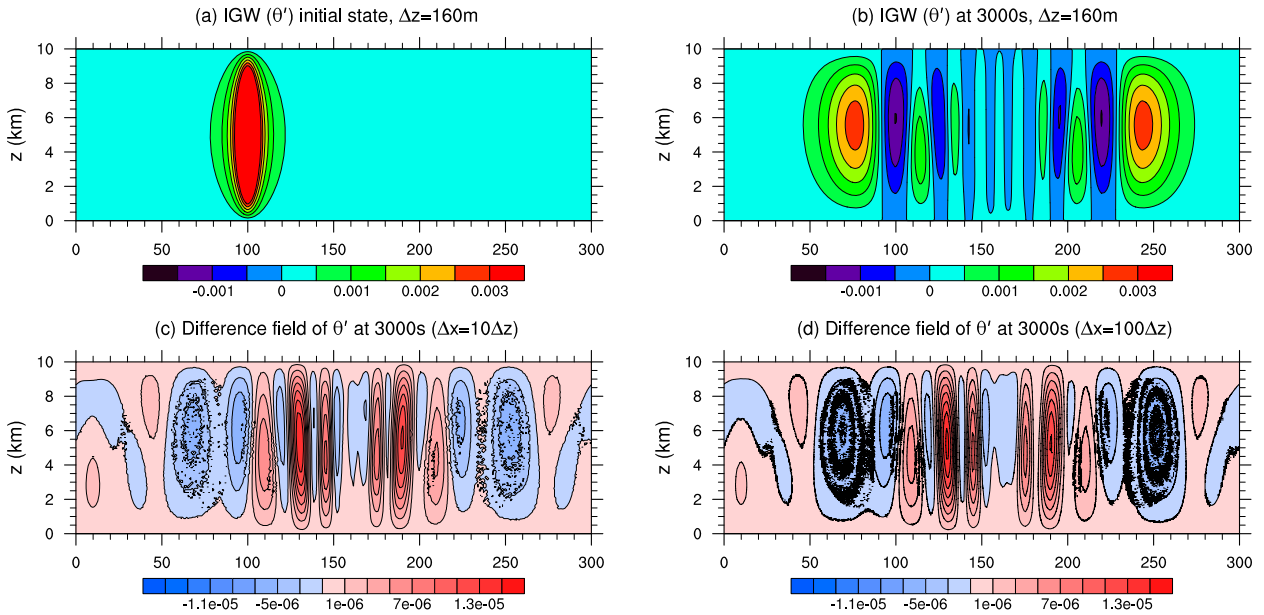The nonhydrostatic inertia–gravity wave (IGW) test introduced by Skamarock and Klemp (1994) serves as

FIG. 3. Numerical solutions (potential temperature perturbation θ') with the IGW test at different aspect ratios $\Delta x/\Delta z = 10, 100$. The P^2-DG scheme with time integrators SSP-RK3 and HEVI schemes are used for the simulation, where Δx is fixed at 1600 m. (a) Initial state of θ' (K) when $\Delta x/\Delta z = 10$, and (b) contour plots of θ' (K) at 3000 s, using SSP-RK3 with $\Delta t = 0.14$ s and $\Delta x/\Delta z = 10$. (c) The difference fields of θ' between SSP-RK3 and HEVI with $\Delta x/\Delta z = 10$, $\Delta t = 0.14$ s using SSP-RK3, and $\Delta t = 1.4$ s using HEVI. (d) As in (c), but for $\Delta x/\Delta z = 100$ and $\Delta t = 0.014$ s using SSP-RK3.

a useful tool to check the accuracy of various time stepping schemes in a more realistic nonhydrostatic setting. This test case obtains the grid-converged solution without the need of a numerical diffusion. We use this experiment to test the accuracy of the HEVI schemes for our DG-NH model under different aspect ratio of grid resolutions. This test examines the evolution of a potential temperature perturbation θ', in a channel with periodic boundary conditions on the lateral boundaries. The initial perturbation (shown in Fig. 3a) radiates to the left and right symmetrically, while being advected to the right with a prescribed mean horizontal flow.

The parameters for the test are the same as the NH test reported in Skamarock and Klemp (1994). The Brunt–Väisälä frequency is given as $N_f = 0.01\,\mathrm{s}^{-1}$, the upper boundary is placed at $z_T = 10$ km, the perturbation half-width is $a_m = 5$ km, and the initial horizontal velocity is $u = 20\,\mathrm{m\,s}^{-1}$. The inertia–gravity waves are produced by an initial potential temperature perturbation (θ') of the following form:

$$\theta' = \theta_c \frac{a_m^2 \sin(\pi z/h_c)}{a_m^2 + (x - x_c)^2}, \qquad (52)$$

where $\theta_c = 0.01$ K, $h_c = 10$ km, and $x_c = 100$ km. The (x, z) domain is defined to be $[0, 300] \times [0, 10]\,\mathrm{km}^2$, with no-flux boundary conditions at the top and bottom of the domain and periodic on the left and right sides. The

IGW simulation is performed for $t_T = 3000$ s. For a moderate aspect ratio $\Delta x/\Delta z = 10$, the numerical solution after 3000 s is shown in Fig. 3b, where the P^2 DG-NH model is integrated with SSP-RK3 time integrator for $\Delta t = 0.14$ s and $\Delta z = 160$ m. We have experimented with DG-NH model for various polynomial orders (P^k, $k = 2, 3, 4$), while fixing the resolution; however, the simulated results are found to be very comparable.

To perform a qualitative comparison of the HEVI scheme versus the SSP-RK3 scheme, we test P^2-DG under two options of aspect ratio $\Delta x/\Delta z = 10, 100$, while fixing $\Delta x = 1600$ m. For SSP-RK3, the CFL stability is constrained by the $\min\{\Delta x, \Delta z\}$, which only allows $\Delta t = 0.14$ s for $\Delta z = 160$ m ($N_x = 63$, $N_z = 21$) and $\Delta t = 0.014$ s for $\Delta z = 16$ m ($N_x = 60$, $N_z = 200$). However, for the HEVI simulation, the CFL condition for the whole system is not dominated by the smaller grid spacing Δz, permitting a larger time step $\Delta t = 1.4$ s, regardless of the choice of Δz. In other words, the time step of HEVI is 10 times the time step of SSP-RK3 when $\Delta x/\Delta z = 10$ and 100 times when $\Delta x/\Delta z = 100$. Figures 3c and 3d show the difference field of the solution (i.e., SSP-RK3 solution minus HEVI solution), when $\Delta x/\Delta z = 10, 100$, respectively. It is observed that the difference is two orders of magnitude smaller than that of θ', and the difference field of $\Delta x/\Delta z = 10$ (Fig. 3c) is slightly less noisy than that of $\Delta x/\Delta z = 100$ (Fig. 3d). For both horizontal-vertical aspect ratios, the range of the potential temperature
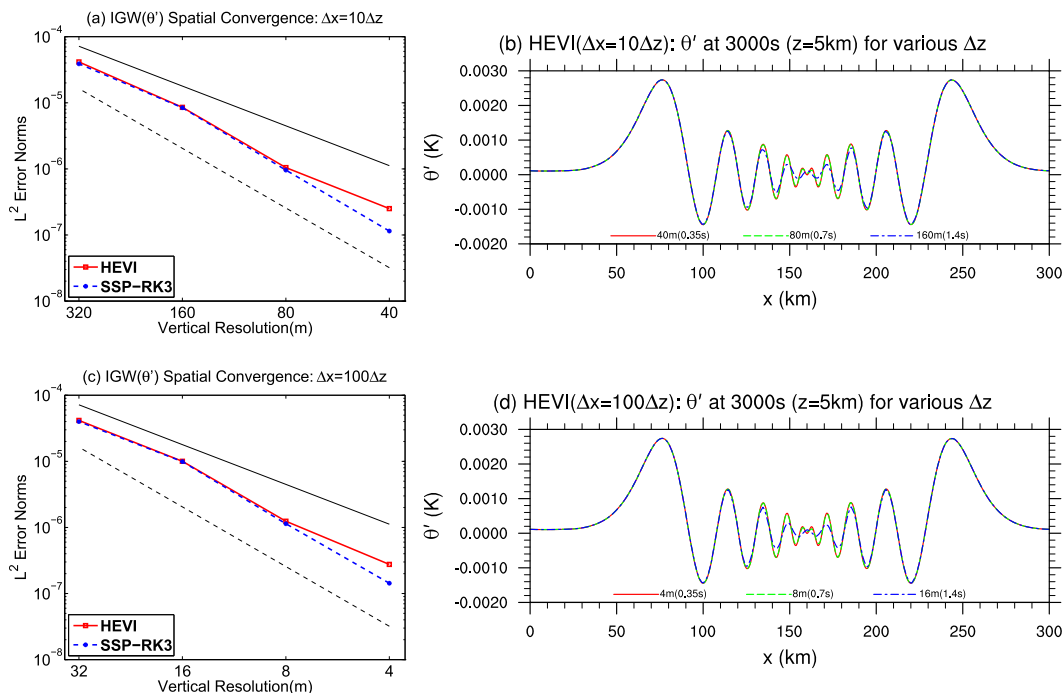
FIG. 4. Spatial convergence of L^2 error for the P^2-DG model employing IGW test with the time integrators HEVI and SSP-RK3, using the aspect ratios $\Delta x/\Delta z = 10$ and 100. The spatial convergence when (a) $\Delta x/\Delta z = 10$ and (c) $\Delta x/\Delta z = 100$. The top solid line and the bottom dashed line correspond to slopes of second- and third-order convergence, respectively. (b),(d) The potential temperature perturbation θ' (K) sampled at $z = 5$ km, at various vertical resolutions for the HEVI simulations. The time step size for each resolution is shown in the parentheses.

perturbation is $\theta' \in [-1.52 \times 10^{-3}, 2.79 \times 10^{-3}]$ K, which is fairly close to the results of Giraldo and Restelli (2008) and Li et al. (2013).

To capture the spatial convergence of the HEVI scheme, we test P^2-DG under two options of aspect ratio $\Delta x/\Delta z = 10$, 100. Since there is no analytic solution available for this test case, the reference solution is chosen from the high-resolution solution of SSP-RK3 with $\Delta x = 200$ m and $\Delta t = 0.0175$ s when $\Delta x = 10\Delta z$ or $\Delta t = 0.001\,75$ s when $\Delta x = 100\Delta z$. Figures 4a and 4c show the convergence rate of the HEVI scheme as well as SSP-RK3 scheme in a range of horizontal resolutions $\{400, 800, 1600, 3200\}$ m for $\Delta x = 10\Delta z$ and $\Delta x = 100\Delta z$, respectively. For the SSP-RK3 scheme, $\Delta t = 0.035$ s when $\Delta x = 10\Delta z$ and $\Delta t = 0.0035$ s when $\Delta x = 100\Delta z$ for $\Delta x = 400$ m. For the HEVI scheme, since the time step for HEVI is only limited by the horizontal grid spacing, $\Delta t = 0.35$ s when $\Delta x = 400$ m, irrelevant of the vertical resolution. For other choices of Δx, Δt scales with Δx linearly. Both Figs. 4a and 4c show third-order convergence of both schemes at a relatively lower resolution, which is anticipated for a P^2-DG scheme, but the HEVI scheme shows a gradually degraded convergence rate at a relatively higher resolution ($\Delta z = 40$ m in Fig. 4a and $\Delta z = 4$ m in Fig. 4c), which may result from the splitting error.

We sample θ' (K) horizontally along $z = 5$ km, as displayed in Fig. 4b for $\Delta x = 10\Delta z$ and Fig. 4d for $\Delta x = 100\Delta z$. In both plots, the distribution is symmetric with respect to the point ($x = 160$ km), which agrees well with the theory, since the horizontal wind ($u = 20$ m s^{-1}) moves the whole field 60 km to the right after 3000 s. It is observed that the HEVI scheme captures fine features of the IGW as the resolution goes higher, while allowing relatively larger Δt, as compared to the SSP-RK3 scheme. This result is also consistent with those reported in Giraldo and Restelli (2008), where a high-order ($k = 8$) DG model was used, and by other recent FV results given in Ahmad and Linedman (2007), Norman et al. (2011), and Li et al. (2013). In addition, there is no visible difference in the convergence rate and the horizontal sampling of θ' for different aspect ratios of horizontal resolution and vertical resolution. This validates our dimensional splitting and assures us that the choice of a higher aspect ratio of grid resolutions does not sacrifice the quality of the numerical solution.

3) DENSITY CURRENT TEST (STRAKA TEST)

The density current benchmark introduced by Straka et al. (1993) is often used to evaluate numerical schemes developed for atmospheric models. The Straka density

current mimics the cold outflow from a convective system and tests a model's ability to control oscillations when run with numerical viscosity. This test involves evolution of a density flow generated by a cold bubble in a neutrally stratified atmosphere. The cold bubble descends to the ground and spreads out in the horizontal direction, forming three Kelvin–Helmholtz shear instability rotors along the cold front surface. This is a test case suitable for testing the LDG diffusion option in our DG-NH model.

The test case uses a hydrostatically balanced basic state on a uniform potential temperature, $\theta_0 = 300\,\text{K}$, and adds the following perturbation in potential temperature:

$$\theta(x, z) = \begin{cases} \theta_0, & \text{if} \quad L(x, z) > 1, \\ \theta_0 + \Delta\theta(\cos[\pi L(x, z)] + 1)/2 & \text{otherwise,} \end{cases} \tag{53}$$

where $L(x, z) = \sqrt{[(x - x_0)/x_r]^2 + [(z - z_0)/z_r]^2}$, $\Delta\theta = -15\,\text{K}$, $(x_r, z_r) = (4, 2)\,\text{km}$, and $(x_0, z_0) = (0, 3)\,\text{km}$. No-flux boundary conditions are applied for all four boundaries. A dynamic viscosity of $\nu = 75\,\text{m}^2\,\text{s}^{-1}$ is used for the diffusion (Straka et al. 1993). The diffusion terms are treated with the LDG approach. The model is integrated for 900 s on a domain $[-26.5, 26.5] \times [0, 6.4]\,\text{km}^2$.

For an equidistant grid ($\Delta x = \Delta z$) there is no particular advantage for HEVI-DG over RK-DG in terms of efficiency, unless $w > u$. The simulated potential temperature θ' (K) after 900 s for the Straka density current is shown in Figs. 5a–d, with the grid spacings successively halved from 200 to 25 m. The time step is $\Delta t = 0.16\,\text{s}$ for 200-m grid resolution and decreases linearly with the grid spacing. The results shown are with the P^2 version of the DG-NH model. This test was repeated with the high-order (P^k, $k = 3, 4$) spatial discretization with a similar resolution, and the results were visually indistinguishable, showing an acceptable grid convergence. It is observed that three Kelvin–Helmholtz rotors develop as the grid resolution is refined. The numerical results are comparable to other published results (Ahmad and Linedman 2007; Norman et al. 2011; Li et al. 2013), despite different contour values. This test verifies the LDG second-order diffusion in an operator-split configuration.

Figure 5e gives the horizontal profile of the potential temperature perturbation θ' sampled along $z = 1.2\,\text{km}$ at the same set of the grid resolutions as in Figs. 5a–d. The three valleys in the right panel of Fig. 5e correspond to the three Kelvin–Helmholtz rotors in Figs. 5a–d. As the resolution goes higher, more fine features of the current are captured reflecting the multiscale nature of the flow. Our results agree well with the multimoment FV

method (Li et al. 2013) and high-order DG method (Giraldo and Restelli 2008). To compare the performance of HEVI and SSP-RK3, the profile of potential temperature perturbation along $z = 1.2\,\text{km}$ for $\Delta z = 100\,\text{m}$ is shown in Fig. 5f. The result of the HEVI scheme is visually in line with that of SSP-RK3, which demonstrates the robustness of the HEVI-DG combined with the LDG diffusion.

4) SCHÄR MOUNTAIN TEST

We consider the Schär mountain test (Schär et al. 2002) to evaluate the performance of our HEVI scheme in handling complex topography. The Schär mountain test simulates the generation of gravity waves by a constant horizontal flow field in a uniform stratified atmosphere impinging on a nonuniform mountain range. The profile of the mountain range is given as

$$h(x) = h_0 \exp\left(-\frac{x^2}{a_0^2}\right) \cos^2\left(\frac{\pi x}{\lambda}\right), \tag{54}$$

where $h_0 = 250\,\text{m}$, $a_0 = 5000\,\text{m}$, and $\lambda = 4000\,\text{m}$. The terrain-following, height-based coordinate in (4) takes effect in this test case and is shown in Fig. 6a. The gravity waves are composed of two major spectral components: the large-scale hydrostatic waves propagate deeply in the vertical, while the small-scale nonhydrostatic waves decay rapidly as the altitude increases.

The initial state of the atmosphere has a constant horizontal flow of $u_0 = 10\,\text{m s}^{-1}$ and the Brunt–Väisälä frequency is $N_f = 0.01\,\text{s}^{-1}$. The reference potential temperature $\bar{\theta}$ can be computed from (47) using $\theta_0 = 280\,\text{K}$. The simulation is carried out in the domain of $[-25, 25] \times [0, 21]\,\text{km}^2$. No-flux boundary conditions are imposed at the bottom boundary and nonreflecting boundary conditions are used along the top, left, and right boundaries. The sponge layers are placed in the region of $\zeta \geq 9\,\text{km}$ with $\tau_{\text{top}} = 0.28$ for the top boundary and $|x| \geq 15\,\text{km}$ with $\tau_{\text{lat}} = 0.18$ for the lateral outflow boundaries. Here P^3-DG is used and the grid resolution is chosen as $\Delta x = 250\,\text{m}$ and $\Delta\zeta = 105\,\text{m}$ ($N_x = 50, N_z = 50$), which leads to $\Delta x/\Delta\zeta \approx 2$. We used a different aspect ratio than the one used in Li et al. (2013), Ullrich and Jablonowski (2012), and Giraldo and Restelli (2008), where $\Delta x/\Delta\zeta \approx 1$, because this makes HEVI scheme more challenging. The simulation time is $t_T = 10\,\text{h}$ (36 000 s) with $\Delta t = 0.125\,\text{s}$ for the HEVI scheme and $\Delta t = 0.065\,\text{s}$ for the SSP-RK3 scheme. Figures 6b and 6c show the contours of the horizontal and vertical wind fields at 10 h in the region $[-10, 10] \times [0, 10]\,\text{km}^2$ for visualization. No visually distinguishable difference is observed between the results of SSP-RK3 scheme and HEVI scheme. There is no unphysical distorted wave
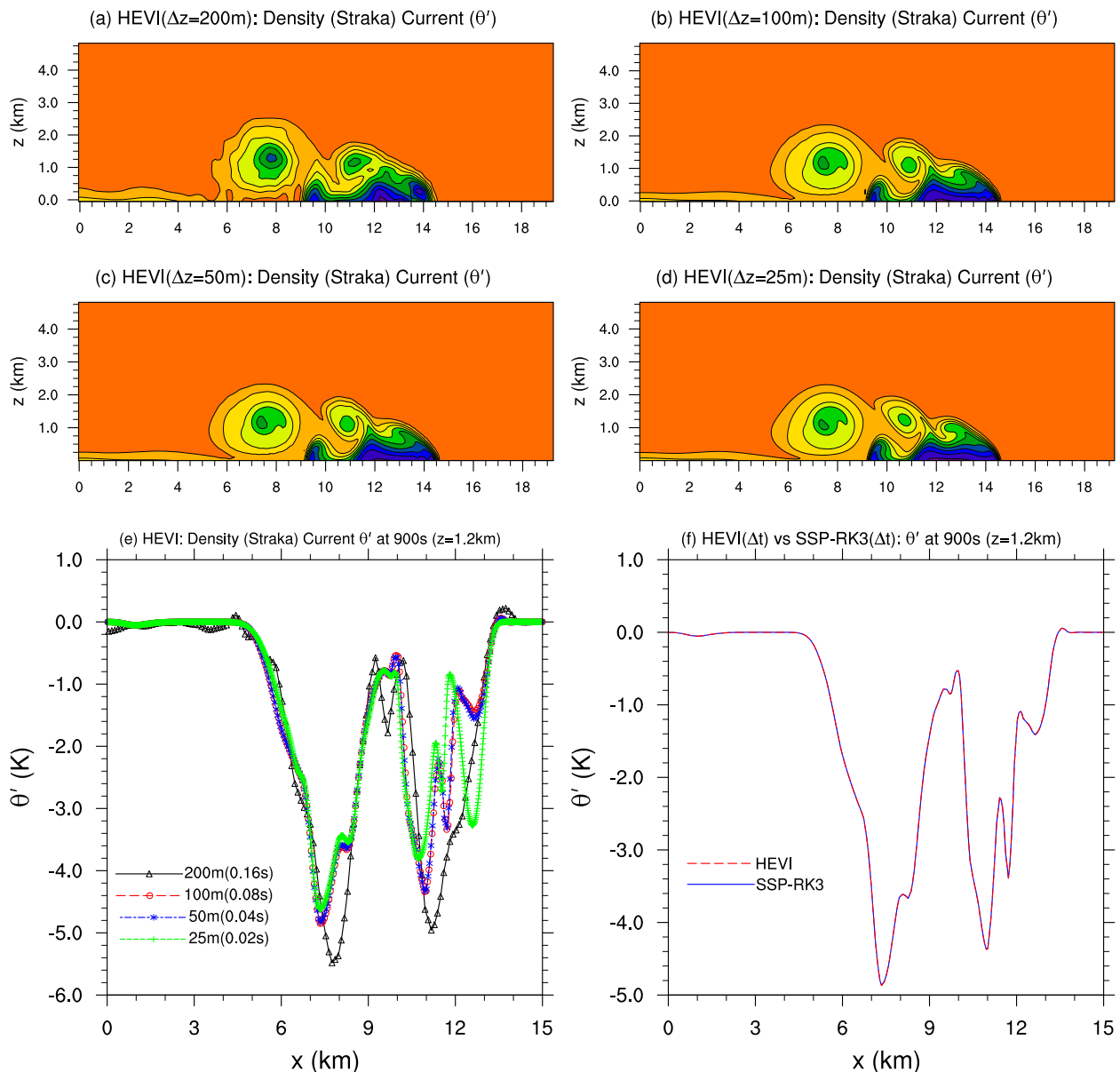
FIG. 5. The plots of potential temperature perturbation θ' (K) for the Straka density current test on a uniform grid $\Delta x = \Delta z$ with P^2-DG schemes for 900-s integration. (a)–(d) The contour plots of θ' using HEVI in a range of resolutions from 200 to 25 m. Time step $\Delta t = 0.16$ s for 200-m grid resolution, and is otherwise proportional with the grid resolution. The contour values (K) are in the range of $[-9.5, 0.5]$ with an increment 1.0. (e),(f) The sampling of θ' at $z = 1.2$ km are shown, where (e) shows the plots corresponding to the resolutions as used in (a)–(d), and the associated time step is given in the parentheses. In (f) HEVI and SSP-RK3 schemes are compared at a resolution of 100 m.

pattern shown in the upper level of the domain, and our results are comparable to the other publications (Li et al. 2013; Ullrich and Jablonowski 2012; Giraldo and Restelli 2008). In addition, our handling of the complex domain does not introduce spurious noise, as discussed in Klemp et al. (2003).

To increase the orographic effects, the height of the mountain in the Schär test is increased to $h_0 = 750$ m, so that the maximum slope for the mountain is about 55%

(Simarro et al. 2013). The purpose of this test is to make a close comparison between HEVI and SSP-RK3 in a relatively extreme case. The grid resolution and boundary conditions for this experiment remain the same as in the Schär test, and the model is integrated for a short period of $t = 1800$ s, with HEVI as well as SSP-RK3 schemes. The terrain-following coordinate is shown in Fig. 6d, which is more curved (with sharp gradients) than the case shown in Fig. 6a. For the HEVI scheme, $\Delta t = 0.125$ s, which is twice
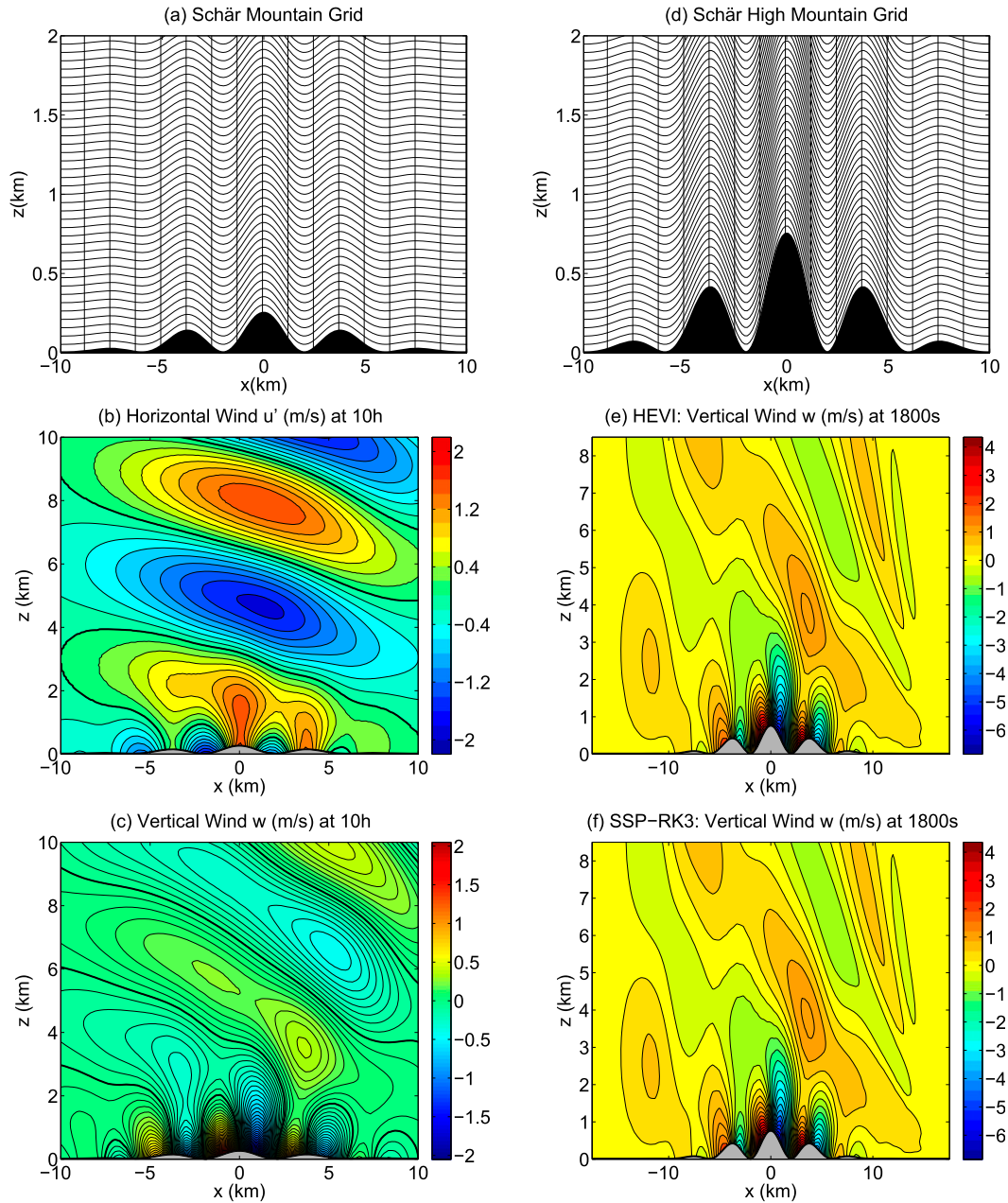
FIG. 6. Numerical results with P^3-DG model combined with HEVI scheme for the Schär mountain test. The mountain profiles and elements: (a) with $h_0 = 250$ m and (d) with $h_0 = 750$ m. The domain is $[-25, 25] \times [0, 21]$ km^2 with grid spacing $\Delta x = 250$ m and $\Delta \zeta = 105$ m. (b),(c) The contour plots (zero contour is highlighted by a thicker line) of wind fields after 10 h of simulation with $\Delta t = 0.125$ s: (b) horizontal wind field perturbation u' (m s^{-1}), with a contour increment 0.2 m s^{-1}, and (c) vertical wind field w (m s^{-1}), with a contour increment 0.05 m s^{-1}. (e),(f) Vertical wind field w (m s^{-1}) with a contour increment 0.3 m s^{-1}: (e) for HEVI scheme and (f) for SSP-RK3 scheme.

the Δt used for SSP-RK3 scheme. The vertical wind field is shown in Figs. 6e,f for the HEVI and SSP-RK3 schemes, respectively. The vertical wind field is virtually indistinguishable between the HEVI and SSP-RK3 schemes, with maximum absolute vertical velocities of 6.45 and 6.44 m s^{-1}, respectively. This again shows that

the HEVI-type dimensional splitting scheme permits a larger time step and it does not introduce additional noise, even in an extreme case, and the results are comparable to that with SSP-RK3 scheme. Although our experimental setup including the boundary conditions and grid resolution is different, the vertical wind

fields shown in Figs. 6e,f are similar to the corresponding Fig. 3 of Simarro et al. (2013).

6. Summary and conclusions

We have proposed a *moderate-order* discontinuous Galerkin nonhydrostatic (DG-NH) model based on the compressible Euler equations in a 2D (x, z) Cartesian plane, with a simple operator-splitting time integration scheme. The model uses a terrain-following height-based coordinate to handle the orography. For the atmospheric simulation on the nonhydrostatic scale, a high aspect ratio between the horizontal and vertical spatial discretization imposes a stringent restriction on the explicit time step size for the Euler system. To alleviate the dominant effect due to large horizontal–vertical aspect ratio, the so-called *horizontally explicit and vertically implicit* (HEVI) scheme via the Strang splitting is proposed and studied in our DG-NH model. The HEVI time-integration scheme avoids the tiny time step limitations, inflicted by the vertical grid spacing ($\Delta z \ll \Delta x$), and, therefore, the overall CFL restriction on the time step is mainly determined by the horizontal grid spacing (Δx).

The accuracy of our HEVI DG-NH model is tested under a suite of NH benchmark test cases. The numerical results, which are in agreement with those in literature, show that the HEVI scheme is robust and capable of relaxing the CFL constraint to the horizontal grid spacing and yields accurate simulations, even though the vertical grid spacing is greatly smaller than the horizontal ($\Delta x/\Delta z = 10, 100$). As expected, a second-order temporal convergence is observed with the HEVI scheme, and a third-order spatial convergence is obtained with the HEVI scheme as well as the SSP-RK3 scheme, which is consistent with the P^2-DG discretization. We have also implemented an LDG-type second-order diffusion in a dimension-split manner to be consistent with the HEVI formulation. The LDG diffusion effectively eliminates the small-scale noise for the model and stabilizes the flow field, as is shown in the Straka density current test. Moreover, in the presence of orography (Schär mountain test), no spurious wave pattern or noise is detected from the results of our HEVI scheme, and the numerical simulation is visually identical to that of the SSP-RK3 scheme.

The HEVI scheme is a practical option and competitive approach for global NH atmospheric modeling, since the existing solver of the horizontal dynamics can be greatly recycled as done in a typical split-explicit case when implemented in a full 3D domain. Here we demonstrate that it is a viable option for the high-order DG method as well. However, the efficiency of the HEVI scheme mainly depends on the performance of the 1D implicit solver. Proper preconditioning is a possible remedy for accelerating the Newton–Krylov Jacobian-free solver, and work in this direction is progressing. Our ultimate goal is to implement the HEVI-DG formulation in the High-Order Method Modeling Environment (HOMME) developed at NCAR, to extend it as a NH framework. The attractive features of HOMME (excellent parallel efficiency) can be exploited for the resulting NH dynamical core when HEVI-DG scheme is implemented. Further investigation will be continued on the application of the HEVI time-split scheme in the HOMME framework.

APPENDIX

Diffusion

Consider the following scalar advection-diffusion equation on an element Ω_e, with the known (constant) diffusion coefficient ν (m^2 s^{-1}):

$$\frac{\partial U}{\partial t} + \mathbf{\nabla} \cdot \mathbf{F}(U) = \nu \nabla^2 U. \tag{A1}$$

We summarize the application of LDG diffusion process in the following steps. [In the following process the subscript $(\cdot)_h$ is dropped for simplicity.]

1) The key idea of the LDG approach is the introduction of a local auxiliary variable $\mathbf{q} = \nu \mathbf{\nabla} U$, and rewriting the above problem as a first-order system:

$$\mathbf{q} - \nu \mathbf{\nabla} U = 0, \tag{A2}$$

$$\frac{\partial U}{\partial t} + \mathbf{\nabla} \cdot \mathbf{F}(U) - \mathbf{\nabla} \cdot \mathbf{q} = 0. \tag{A3}$$

2) For the LDG method, Let the numerical fluxes U^*, $\mathbf{q}^*$ in (A6) be evaluated in terms of jump $[\cdot]$ and central $\{\cdot\}$ fluxes, defined as follows:

$$U^* = \{U\} + \boldsymbol{\beta} \cdot [U], \quad \mathbf{q}^* = \{\mathbf{q}\} - \boldsymbol{\beta}[\mathbf{q}] - \eta_k[U], \tag{A4}$$

$$\{U\} = (U^+ + U^-)/2, [U] = (U^- - U^+)\mathbf{n};$$
$$\{\mathbf{q}\} = (\mathbf{q}^+ + \mathbf{q}^-)/2, [\mathbf{q}] = (\mathbf{q}^- - \mathbf{q}^+) \cdot \mathbf{n}.$$

3) Discretize the above system in (A2) and (A3) using the weak formulation (Green's method). This is done by first multiplying by a vector test function $\Phi \in \mathcal{V}^d(\Omega)$ (d is the dimension of the problem) in (A2) and integrating by parts:

$$\int_\Omega \mathbf{q} \cdot \Phi \, d\Omega = \nu \left[\int_{\partial\Omega} U^*\Phi \cdot \mathbf{n} \, d\sigma - \int_\Omega U\mathbf{\nabla} \cdot \Phi \, d\Omega \right].$$
(A5)

4) The final weak formulation for the advection–diffusion equation (A1) is obtained by using a test function $[\varphi \in \mathcal{V}(\Omega)]$, the Lax–Friedrichs flux $\hat{\mathbf{F}}$, and combining (A5):

$$\frac{\partial}{\partial t} \int_\Omega U\varphi \, d\Omega - \int_\Omega \mathbf{F}(U) \cdot \mathbf{\nabla}\varphi \, d\Omega + \int_{\partial\Omega} \hat{\mathbf{F}}(U) \cdot \mathbf{n}\varphi \, d\sigma$$
$$+ \nu \int_\Omega \mathbf{q} \cdot \mathbf{\nabla}\varphi \, d\Omega - \nu \int_{\partial\Omega} \mathbf{q}^* \cdot \mathbf{n}\varphi \, d\sigma = 0.$$
(A6)

5) In practice this is done in two stages. First, evaluate $\mathbf{q}$ in (A5) using the above fluxes and then evaluate (A6).

Note that various second-order diffusions can be formulated by carefully choosing the parameter values $\boldsymbol{\beta}$ and η_k, which are BR2, Bauman–Oden, and "flip-flop," etc. [see Cockburn and Shu (1998) for multiple variants of the LDG method]. The constants $\boldsymbol{\beta} = \mathbf{n}/2$ and $\eta_k = 0$ are set for most test cases considered herein, nevertheless, other options are available in the DG-NH model.

REFERENCES

Ahmad, N., and J. Linedman, 2007: Euler solutions using flux-based wave decomposition. *Int. J. Numer. Methods Fluids,* **54,** 47–72, doi:10.1002/fld.1392.

Alexander, R., 1977: Diagonally implicit Runge–Kutta methods for stiff O.D.E.'s. *SIAM J. Numer. Anal.,* **14,** 1006–1021, doi:10.1137/0714068.

Ascher, U. M., S. J. Ruuth, and R. J. Spiteri, 1997: Implicit-explicit Runge–Kutta methods for time-dependent partial differential equations. *Appl. Numer. Math.,* **25,** 151–167, doi:10.1016/S0168-9274(97)00056-1.

Bao, L., R. D. Nair, and H. M. Tufo, 2014: A mass and momentum flux-form high-order discontinuous Galerkin shallow water model on the cubed-sphere. *J. Comput. Phys.,* **271,** 224–243, doi:10.1016/j.jcp.2013.11.033.

Brdar, S., M. Baldauf, A. Dedner, and R. Klöfkorn, 2013: Comparison of dynamical cores for NWP models: Comparison of COSMO and Dune. *Theor. Comput. Fluid Dyn.,* **27,** 453–472, doi:10.1007/s00162-012-0264-z.

Butcher, J. C., 1987: *The Numerical Analysis of Ordinary Differential Equations: Runge–Kutta and General Linear Methods.* John Wiley & Sons Inc., 528 pp.

Clark, T. L., 1977: A small-scale dynamics model using a terrain-following coordinate transformation. *J. Comput. Phys.,* **24,** 186–215, doi:10.1016/0021-9991(77)90057-2.

Cockburn, B., 1997: An introduction to the discontinuous-Galerkin method for convection-dominated problems. *Lecture Notes in Mathematics: Advanced Numerical Approximation of Nonlinear Hyperbolic Equations,* A. Quarteroni, Ed., Vol. 1697, Springer, 151–268.

——, and C.-W. Shu, 1998: The local discontinuous Galerkin for convection diffusion systems. *SIAM J. Numer. Anal.,* **35,** 2440–2463, doi:10.1137/S0036142997316712.

Dennis, J. M., and Coauthors, 2012: CAM-SE: A scalable spectral element dynamical core for the Community Atmosphere Model. *Int. J. High Perform. Comput. Appl.,* **26,** 74–89, doi:10.1177/1094342011428142.

Durran, D. R., 1999: *Numerical Methods for Wave Equations in Geophysical Fluid Dynamics.* Springer, 465 pp.

——, and J. B. Klemp, 1983: A compressible model for the simulation of moist mountain waves. *Mon. Wea. Rev.,* **111,** 2341–2361, doi:10.1175/1520-0493(1983)111<2341:ACMFTS>2.0.CO;2.

Gal-Chen, T., and R. C. Sommerville, 1975: On the use of a coordinate transformation for the solution of Navier–Stokes. *J. Comput. Phys.,* **17,** 209–228, doi:10.1016/0021-9991(75)90037-6.

Giraldo, F. X., and M. Restelli, 2008: A study of spectral element and discontinuous Galerkin methods for the Navier–Stokes equations in nonhydrostatic mesoscale atmospheric modeling: Equation sets and test cases. *J. Comput. Phys.,* **227,** 3849–3877, doi:10.1016/j.jcp.2007.12.009.

——, J. F. Kelly, and E. M. Constantinescu, 2013: Implicit-explicit formulations of a three-dimensional nonhydrostatic unified model of the atmosphere (NUMA). *SIAM J. Sci. Comput.,* **35,** B1162–B1194, doi:10.1137/120876034.

Gottlieb, S., C.-W. Shu, and E. Tadmor, 2001: Strong stability-preserving high-order time discretization methods. *SIAM Rev.,* **43,** 89–112, doi:10.1137/S003614450036757X.

Guo, W., R. D. Nair, and J.-M. Qiu, 2014: A conservative semi-Lagrangian discontinuous Galerkin scheme on the cubed sphere. *Mon. Wea. Rev.,* **142,** 457–475, doi:10.1175/MWR-D-13-00048.1.

Karniadakis, G. E., and S. Sherwin, 2005: *Spectral/hp Element Methods for Computational Fluid Dynamics.* Oxford University Press, 657 pp.

Klemp, J. B., 2011: A terrain-following coordinate with smoothed coordinate surfaces. *Mon. Wea. Rev.,* **139,** 2163–2169, doi:10.1175/MWR-D-10-05046.1.

——, W. C. Skamarock, and O. Fuhrer, 2003: Numerical consistency of metric terms in terrain-following coordinates. *Mon. Wea. Rev.,* **131,** 1229–1239, doi:10.1175/1520-0493(2003)131<1229:NCOMTI>2.0.CO;2.

Knoll, D. A., and D. E. Keyes, 2004: Jacobian-free Newton–Krylov methods: A survey of approaches and applications. *J. Comput. Phys.,* **193,** 357–397, doi:10.1016/j.jcp.2003.08.010.

Li, X., C. Chen, X. Shen, and F. Xiao, 2013: A multimoment constrained finite-volume model for nonhydrostatic atmospheric dynamics. *Mon. Wea. Rev.,* **141,** 1216–1240, doi:10.1175/MWR-D-12-00144.1.

Liska, R., and B. Wendroff, 2003: Comparison of several difference schemes on 1D and 2D test problems for the Euler equations. *SIAM J. Sci. Comput.,* **25,** 995–1017, doi:10.1137/S1064827502402120.

Lock, S. J., N. Wood, and H. Weller, 2014: Numerical analyses of Runge–Kutta implicit-explicit schemes for horizontally explicit, vertically implicit solutions of atmospheric models. *Quart. J. Roy. Meteor. Soc.,* **140,** 1654–1669, doi:10.1002/qj.2246.

Melvin, T., M. Dubal, N. Wood, A. Staniforth, and M. Zerroukat, 2010: An inherently mass-conserving iterative semi-implicit

semi-Lagrangian discretization of the non-hydrostatic vertical-slice equations. *Quart. J. Roy. Meteor. Soc.,* **136,** 799–814, doi:10.1002/qj.603.

Michalakes, J., and Coauthors, 2007: WRF nature run. *Proc. 2007 ACM/IEEE Conf. on Supercomputing, 2007 (SC' 07),* Reno, NV, ACM; IEEE, 1–6, doi:10.1145/1362622.1362701.

Nair, R. D., 2009: Diffusion experiments with a global discontinuous Galerkin shallow-water model. *Mon. Wea. Rev.,* **137,** 3339–3350, doi:10.1175/2009MWR2843.1.

——, H.-W. Choi, and H. M. Tufo, 2009: Computational aspects of a scalable high-order discontinuous Galerkin atmospheric dynamical core. *Comput. Fluids,* **38,** 309–319, doi:10.1016/j.compfluid.2008.04.006.

——, M. N. Levy, and P. H. Lauritzen, 2011: Emerging numerical methods for atmospheric modeling. *Numerical Techniques for Global Atmospheric Models,* P. H. Lauritzen et al., Eds., Vol. 80, Springer-Verlag, 189–250.

Norman, M. R., R. D. Nair, and F. H. M. Semazzi, 2011: A low communication and large time step explicit finite-volume solver for non-hydrostatic atmospheric dynamics. *J. Comput. Phys.,* **230,** 1567–1584, doi:10.1016/j.jcp.2010.11.022.

Prusa, J., P. Smolarkiewicz, and A. Wyszogrodzki, 2008: EULAG, a computational model for multiscale flows. *Comput. Fluids,* **37,** 1193–1207, doi:10.1016/j.compfluid.2007.12.001.

Restelli, M., and F. Giraldo, 2009: A conservative discontinuous Galerkin semi-implicit formulation for the Navier–Stokes equations in nonhydrostatic mesoscale modeling. *SIAM J. Sci. Comput.,* **31,** 2231–2257, doi:10.1137/070708470.

Saad, Y., and M. H. Schultz, 1986: GMRES: A generalized minimal residual algorithm for solving nonsymmetric linear systems. *SIAM J. Sci. Stat. Comput.,* **7,** 856–869, doi:10.1137/0907058.

Satoh, M., 2002: Conservative scheme for the compressible nonhydrostatic models with the horizontally explicit and vertically implicit time integration scheme. *Mon. Wea. Rev.,* **130,** 1227–1245, doi:10.1175/1520-0493(2002)130<1227:CSFTCN>2.0.CO;2.

Schär, C., D. Leuenberger, O. Fuhrer, D. Luthic, and C. Girard, 2002: A new terrain-following vertical coordinate formulation for atmospheric prediction models. *Mon. Wea. Rev.,* **130,** 2459–2480, doi:10.1175/1520-0493(2002)130<2459:ANTFVC>2.0.CO;2.

Simarro, J., V. Homar, and G. Simarro, 2013: A non-hydrostatic global spectral dynamical core using a height-based vertical coordinate. *Tellus,* **65A,** 20270, doi:10.3402/tellusa.v65i0.20270.

Skamarock, W., and J. Klemp, 1994: Efficiency and accuracy of the Klemp–Wilhelmson time-splitting technique. *Mon. Wea. Rev.,*

122, 2623–2630, doi:10.1175/1520-0493(1994)122<2623:EAAOTK>2.0.CO;2.

——, and ——, 2008: A time-split nonhydrostatic atmospheric model for weather research and forecasting applications. *J. Comput. Phys.,* **227,** 3465–3485, doi:10.1016/j.jcp.2007.01.037.

——, ——, M. G. Duda, L. D. Flower, S.-H. Park, and T. D. Ringler, 2012: A multiscale nonhydrostatic atmospheric model using centroidal Voronoi tesselations and C-grid staggering. *Mon. Wea. Rev.,* **140,** 3090–3105, doi:10.1175/MWR-D-11-00215.1.

St-Cyr, A., and D. Neckels, 2009: A fully implicit Jacobian-free high-order discontinuous Galerkin mesoscale flow solver. *Lecture Notes in Computer Science,* G. Allen et al., Eds., Vol. 5545, Springer-Verlag, 243–252, doi:10.1007/978-3-642-01973-9_28.

Straka, J., R. Wilhelmson, L. Wicker, J. Anderson, and K. Droegemeier, 1993: Numerical solutions of a non-linear density current: A benchmark solution and comparisons. *Int. J. Numer. Methods Fluids,* **17,** 1–22, doi:10.1002/fld.1650170103.

Strang, G., 1968: On the construction and comparison of difference schemes. *SIAM J. Numer. Anal.,* **5,** 506–517, doi:10.1137/0705041.

Tomita, H., K. Goto, and M. Satoh, 2008: A new approach to atmospheric general circulation model: Global cloud resolving model NICAM and its computational performance. *SIAM J. Sci. Comput.,* **30,** 2755–2776, doi:10.1137/070692273.

Toro, E. F., 1999: *Riemann Solvers and Numerical Methods for Fluid Dynamics: A Practical Introduction.* 2nd ed. Springer-Verlag, 724 pp.

Toy, M. D., and D. A. Randall, 2009: Design of a nonhydrostatic atmospheric model based on a generalized vertical coordinate. *Mon. Wea. Rev.,* **137,** 2305–2330, doi:10.1175/2009MWR2834.1.

Ullrich, P., and C. Jablonowski, 2012: Operator-split Runge–Kutta–Rosenbrock methods for nonhydrostatic atmospheric models. *Mon. Wea. Rev.,* **140,** 1257–1284, doi:10.1175/MWR-D-10-05073.1.

Weller, H., S.-J. Lock, and N. Wood, 2013: Runge–Kutta IMEX schemes for the Horizontally Explicit/Vertically Implicit (HEVI) solution of wave equations. *J. Comput. Phys.,* **252,** 365–381, doi:10.1016/j.jcp.2013.06.025.

Zhang, Y., and R. D. Nair, 2012: A nonoscillatory discontinuous Galerkin transport scheme on the cubed sphere. *Mon. Wea. Rev.,* **140,** 3106–3126, doi:10.1175/MWR-D-11-00287.1.